J. Fluid Mech. (2024), *vol.* 984, A2, doi:10.1017/jfm.2024.103

JFM PAPERS

Hydrodynamics and scaling laws for intermittent S-start swimming

Dewu Yang[1,2], Jie Wu[1,†], Kaustubh Khedkar[3], Li-Ming Chao[4,†] and Amneet Pal Singh Bhalla[3,†]

[1]Key Laboratory of Unsteady Aerodynamics and Flow Control, Ministry of Industry and Information Technology, Department of Aerodynamics, Nanjing University of Aeronautics and Astronautics, Nanjing 210016, PR China

[2]School of Aeronautics and Astronautics, Shanghai Jiao Tong University, Shanghai 200240, PR China

[3]Department of Mechanical Engineering, San Diego State University, San Diego, CA 92182, USA

[4]School of Mechanical Engineering and Automation, Harbin Institute of Technology (Shenzhen), Shenzhen 518055, PR China

(Received 3 April 2023; revised 10 January 2024; accepted 25 January 2024)

The hydrodynamics of a self-propelling swimmer undergoing intermittent S-start swimming are investigated extensively with varying duty cycle DC, swimming period T, and tailbeat amplitude A. We find that the steady time-averaged swimming speed $\bar{U}_x$ increases directly with A, but varies inversely with DC and T, where there is a maximal improvement of 541.29 % over continuous cruising swimming. Our results reveal two scaling laws, in the form of input versus output relations, that relate the swimmer's kinematics to its hydrodynamic performance: swimming speed and efficiency. A smaller DC causes increased fluctuations in the swimmer's velocity generation. A larger A, on the other hand, allows the swimmer to reach steady swimming more quickly. Although we set out to determine scaling laws for intermittent S-start swimming, these scaling laws extend naturally to burst-and-coast and continuous modes of swimming. Additionally, we have identified, categorized and linked the wake structures produced by intermittent S-start swimmers with their velocity generation.

Key words: swimming/flying

1. Introduction

Predator–prey behaviour on land, in the air and on water is a fascinating natural phenomenon. For example, to escape from a pursuer, a swimming fish can reach more than ten times gravitational acceleration with only a 30 cm long body by using fast-start propulsion (Triantafyllou, Weymouth & Miao 2016). Indeed, humans look up to the

† Email addresses for correspondence: wuj@nuaa.edu.cn, chaoliming92@gmail.com, asbhalla@sdsu.edu

fast-starting techniques of aquatic animals and hope to apply them to launch bio-inspired underwater robots.

Two fast-starting strategies are usually employed by swimmers, the C- and S-start, according to the bending shape of the swimmer. The S-start propulsion strategy allows the prey to remain in its initial swimming direction and win the pursuit–evasion game. It differs from the C-start strategy, which causes the fish to rotate and change its initial orientation (Weihs 1973). Besides serving as an escape response, S-start behaviour is also used during prey strikes (Domenici & Blake 1997). Recently, much effort has been put into understanding the hydrodynamics of C-start swimming (e.g. Borazjani *et al.* 2012; Gazzola, Rees & Koumoutsakos 2012; Li *et al.* 2014), while little is known about the S-start motion (Triantafyllou 2012).

We conducted a biological experiment on zebrafish (*Danio rerio*) to better understand S-start swimming. The experiment uses zebrafish with body length 3 cm. Experiments are carried out in a cubic water tank of dimensions 50 cm × 3 cm × 3 cm. In the water tank, the top is open for taking movies, and the bottom is illuminated by LEDs. High-speed cameras are used to track fish movement. A sufficient amount of lighting is used to create a well-lit environment for recording movies. Interestingly, we find that the locomotion of zebrafish generally consists of two phases: an S-start swimming phase for providing initial acceleration, followed by a gliding phase for saving energy (see supplementary movie 1 available at https://doi.org/10.1017/jfm.2024.103). In this study, we refer to the combined locomotive gait as intermittent S-start swimming.

The trajectories of swimming zebrafish during intermittent S-start and continuous swimming were analysed, and we observed distinct behaviour (see figure 1(*d*) and supplementary movie 1). In S-starts, zebrafish displayed more frequent tail undulations (characterized by a shorter period T_s), resulting in pronounced lateral movements. This is followed by a glide phase (T_g) without noticeable lateral motion. The continuous swimming of zebrafish displayed a lower tail undulation frequency or longer swimming period T. For S-start swimming, the total period T can be decomposed into an initial S-start phase of period T_s, which is followed by a gliding phase of period T_g, i.e. $T = T_s + T_g$ (figure 1*b*). In chase–escape scenarios, zebrafish benefit from a higher undulation frequency in the S-start phase. During the gliding phase, energy may be conserved, or this behaviour may develop passively as a result of elevated oxygen consumption rates during S-starts (Brett & Sutherland 1965).

Intermittent S-start swimming shares kinematic characteristics with burst-and-coast (B-and-C) swimming (Gleiss *et al.* 2011; Dai *et al.* 2018). A B-and-C swimming strategy involves an undulating burst phase with time period T_{burst}, and a non-undulating coast phase with time period T_{coast} (figure 1*c*). In B-and-C swimming, swimmers employ the same swimming frequency as in continuous swimming, i.e. $T_{burst} = T$ (figures 1*a*,*c*). A B-and-C swimming strategy is usually adopted to conserve energy, characterized by low swimming speeds (Chuang 2009; Floryan, Van Buren & Smits 2017; Akoz & Moored 2018; Akoz *et al.* 2019; Liu, Huang & Lu 2020; Ashraf, Wassenbergh & Verma 2021; Gupta *et al.* 2021; Li *et al.* 2021). S-start swimming, on the other hand, is characterized by higher swimming frequencies, with swimmers striving for higher swimming speeds rather than enhanced efficiency.

As S-start swimming plays an important role in predator–prey behaviour, some questions arise naturally. How do kinematic parameters, such as tailbeat amplitude A, duty cycle DC, and swimming period T, influence the swimming performance (speed and energy consumption) of intermittent S-start swimmers? Do scaling laws apply to intermittent S-start swimming as they do to continuous swimming? What kind of wake

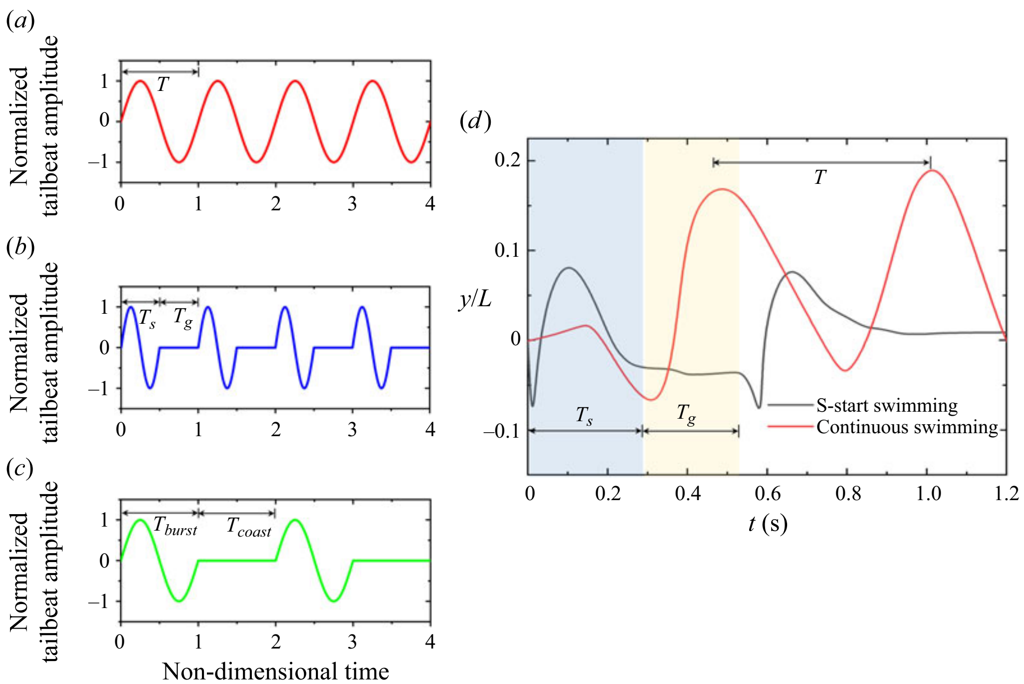

Figure 1. Kinematics of (*a*) continuous, (*b*) S-start, and (*c*) burst-and-coast swimming. (*d*) Real-time motion of the zebrafish tail tracked during S-start and continuous swimming. In (*a*,*d*), T denotes the time period of continuous swimming; T_s and T_g in (*b*,*d*) describe the time period of the S-start and gliding phase in the intermittent S-start swimming, respectively; T_{burst} and T_{coast} in (*c*) refer to the time period of the burst and coast phases in the burst-and-coast swimming, respectively. In (*d*), y is the time-dependent tailbeat amplitude, $L = 3$ cm is the body length, and t is time.

structures are generated by intermittent S-start swimmers? We attempt to address these questions by simulating numerically self-propelling foils undergoing intermittent S-start swimming. Despite the fact that we set out to determine scaling laws for intermittent S-start swimming, these scaling laws apply to S-start, B-and-C and continuous swimming as well.

2. Problem description and methodology

We consider a computational model in which a fish-like NACA0012 foil self-propels right to left in a rectangular domain. The foil can move freely in both horizontal x and vertical/lateral y directions (figure 2*a*). Figure 2(*b*) shows the foil's length as $L = 1$ cm, and its tailbeat amplitude as A. The intermittent S-start swimming is derived from the following kinematics:

$$y(x,t) = \begin{cases} S(t)\, A_m(x) \sin\left[2\pi\left(\dfrac{x}{\lambda} - \dfrac{t}{T_s}\right) - \dfrac{2\pi}{\lambda}\right], & 0 \le t \le T_s, \\ 0, & T_s < t \le T, \end{cases} \tag{2.1}$$

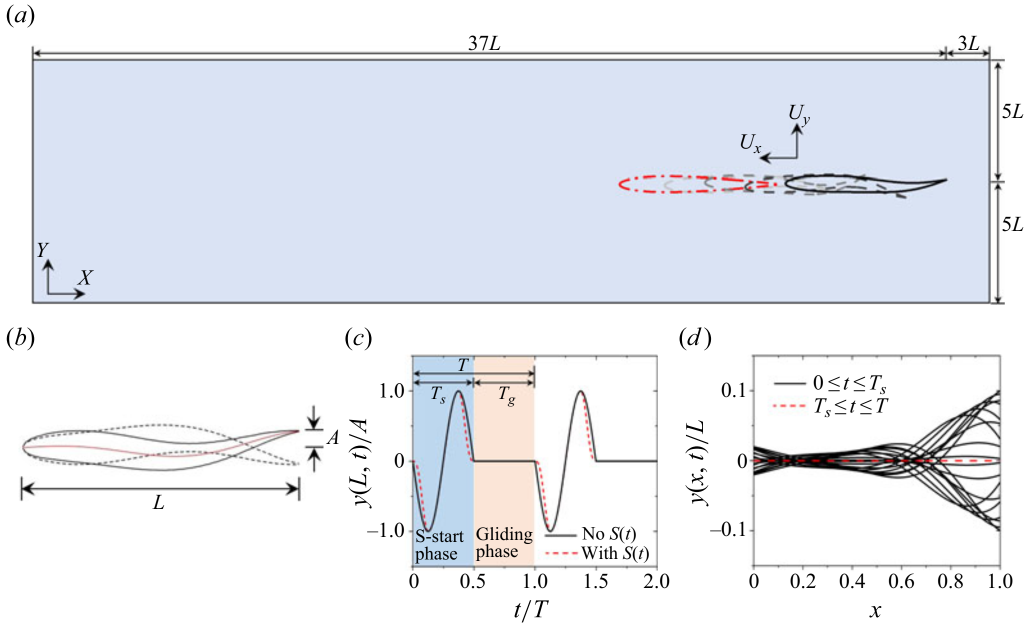

Figure 2. (*a*) Sketch of the computational domain; (*b*) NACA0012 foil; (*c*) intermittent S-start motion; and (*d*) foil's centreline envelope.

in which the smoothing function $S(t)$, given by

$$S(t) = \begin{cases} 0.5\left[1 - \cos\left(\dfrac{4\pi t}{T_s}\right)\right], & 0 \le t \le 0.25T_s, \\ 1, & 0.25T_s < t \le 0.75T_s, \\ 0.5\left[1 - \cos\left(\dfrac{4\pi t}{T_s}\right)\right], & 0.75T_s < t \le T_s, \end{cases} \tag{2.2}$$

is employed to avoid discontinuous accelerations at the junction of the S-start and gliding phase (figure 2*c*). In the equations above, $A_m(x) = a_0 \times (0.02 - 0.08x + 0.16x^2)$ denotes the amplitude function (Videler & Hess 1984) so that $A = A_m(L)$, t is the time, $\lambda = L$ is the wavelength of the travelling wave, T_s denotes the period of the S-start phase, and T is the total swimming period that includes both the S-start and the gliding phase. The envelope of the foil's centreline using (2.1) is shown in figure 2(*d*).

Three non-dimensional numbers are considered in this work: duty cycle (Akoz & Moored 2018)

$$DC = \frac{S\text{-start period}}{\text{total swimming period}} = \frac{T_s}{T}, \tag{2.3}$$

swimming number (Gazzola, Argentina & Mahadevan 2014)

$$Sw = \frac{2\pi LA}{T\nu}, \tag{2.4}$$

and energy consumption coefficient

$$C_E = \frac{CoT}{\rho \nu^2}\left(\frac{L}{W}\right). \tag{2.5}$$

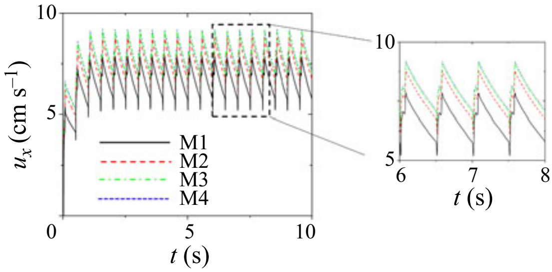

Figure 3. Grid convergence study using four grids, M1 to M4.

Grid	$\Delta x/L$	$\bar{U}_x$ (cm s^{-1})	$\Delta\bar{U}_x$ (%)
M1	5.00×10^{-3}	6.6808	12.376
M2	2.00×10^{-3}	7.6244	4.016
M3	1.25×10^{-3}	7.9434	0.950
M4	1.00×10^{-3}	8.0196	—

Table 1. Grid convergence study with $\Delta t = 10^{-4}T$.

Here, $\nu = 0.0091$ poise is the fluid kinematic viscosity, $\rho = 1$ g cm^{-3} is the density of the fluid, and W is the width of the swimmer into the plane of the paper. In (2.5), CoT denotes the cost of transport, which describes the energy consumption of a self-propelling body. There are two common definitions of CoT – metabolic and mechanical. Here, we focus on the mechanical CoT, which is the ratio of time-averaged total power and time-averaged swimming speed (in the horizontal x direction) (Bale *et al.* 2014). The Reynolds number is defined as $Re = \bar{U}_x L/\nu$.

Numerical investigations are conducted using the open-source IBAMR software, which is a distributed-memory parallel implementation of the immersed boundary (IB) method that incorporates the Cartesian grid adaptive mesh refinement (AMR) technique (Griffith 2009; Griffith & Patankar 2020). The IBAMR software has been used extensively to study fish-like swimming (e.g. Bhalla, Griffith & Patankar 2013*b*; Tytell *et al.* 2016; Hoover *et al.* 2018). The computational domain is taken to be a rectangular box of size $40L \times 10L$ with periodic boundary conditions along the axial direction and no-slip boundary conditions in the lateral direction (figure 2*a*).

A grid convergence study is conducted for an intermittent S-start swimmer with $(DC, T, A/L, \lambda/L) = (0.2, 0.5$ s$, 0.2, 1.0)$. Here, s denotes seconds. The simulations are conducted on four grids (M1 to M4) with uniform mesh spacings $\Delta x/L = \Delta y/L = 5.00 \times 10^{-3}$ (M1), 2.00×10^{-3} (M2), 1.25×10^{-3} (M3) and 1.00×10^{-3} (M4) in the finest level. The time step size is fixed at $\Delta t = 1.00 \times 10^{-4}T$. In figure 3, the time history of swimming velocity u_x is presented for the four grids. Table 1 lists the steady swimming speed $\bar{U}_x$. There is a relatively small difference between M3 and M4 in terms of $\bar{U}_x$ (0.95 %). For the remainder of the simulations, mesh M3 is selected.

Using M3, a time step size convergence study is performed by selecting four values of Δt: $\Delta t1 = 5.00 \times 10^{-4}T$, $\Delta t2 = 2.50 \times 10^{-4}T$, $\Delta t3 = 1.00 \times 10^{-4}T$ and $\Delta t4 = 0.50 \times 10^{-4}T$. Table 2 lists the corresponding $\bar{U}_x$ values. The difference between $\bar{U}_x$ using $\Delta t3$ and $\Delta t4$ is only 0.01 %. Grid M3 and time step size $\Delta t3$ are selected for the remainder of the simulations based on accuracy and computational resources. More convergence studies

Time step size	$\Delta t/T$	$\bar{U}_x$ (cm s^{-1})	$\Delta\bar{U}_x$ (%)
$\Delta t1$	5.00×10^{-4}	7.9475	0.034
$\Delta t2$	2.50×10^{-4}	7.9448	0.018
$\Delta t3$	1.00×10^{-4}	7.9434	0.010
$\Delta t4$	0.50×10^{-4}	7.9426	—

Table 2. Time step size convergence study using grid M3 with $\Delta x/L = \Delta y/L = 1.25 \times 10^{-3}$.

Sw A/L	T(s)						
	0.50	0.75	1.00	1.25	1.50	1.75	2.00
0.05	6283.19	4188.79	3141.59	2513.27	2094.40	1795.20	1570.80
0.10	12566.37	8377.58	6283.19	5026.55	4188.79	3590.39	3141.59
0.15	18849.56	12566.37	9424.78	7539.82	6283.19	5385.59	4712.39
0.20	25132.74	16755.16	12566.37	10053.10	8377.58	7180.78	6283.19

Table 3. *Sw* values for various A and T.

related to the IB method can be found in our previous works (e.g. Bhalla *et al.* 2013*a*; Patel, Bhalla & Patankar 2018).

3. Results and discussions

The hydrodynamics of intermittent S-start swimming is investigated by measuring the swimming speed and the energy consumption associated with a self-propelling foil for $DC = 0.20$–1.00 with $\Delta DC = 0.20$, $T = 0.50$–2.00 s with $\Delta T = 0.25$ s, and $A = 0.05$–$0.20L$ with $\Delta A = 0.05L$. The calculated values of *Sw* corresponding to different pairs of A and T are listed in table 3. We discuss first hydrodynamic performance, then scaling laws, and finally classify the wake structures of an intermittent S-start swimmer. The trends of hydrodynamic performance (swimming speed and *CoT*) are plotted in dimensional units. This avoids confusion related to non-dimensionalization and ensures reproducibility. Eventually, hydrodynamic performance metrics are expressed non-dimensionally through scaling laws in § 3.2.

3.1. *Hydrodynamic performance*

Figure 4 illustrates how DC, T and A affect the steady time-averaged swimming speed $\bar{U}_x$ of the foil. At a given A, $\bar{U}_x$ decreases with increasing T and DC, with maximal and minimal values achieved at $(DC, T, A/L) = (0.20, 0.05\ \text{s}, 0.20)$ and $(DC, T, A/L) = (1.00, 2.00\ \text{s}, 0.05)$, respectively. Depending on DC, as much as 122.89 % to 541.29 % can be gained with intermittent S-start swimming ($DC < 1.0$) compared to the continuous swimming case ($DC = 1.0$); a smaller DC results in higher $\bar{U}_x$. For a given $T_s = T \times DC$, it can also be observed that the intermittent S-start swimming with a larger DC and smaller T produces higher $\bar{U}_x$ than that with a smaller DC and larger T; for example, $\bar{U}_x = 1.47$ cm s^{-1} derived from $(DC, T, A/L) = (0.40, 0.50\ \text{s}, 0.05)$ is larger than $\bar{U}_x = 1.02$ cm s^{-1} for $(DC, T, A/L) = (0.20, 1.00\ \text{s}, 0.05)$, as shown in figure 4(*a*). Due to a longer deceleration period in the gliding phase, a smaller DC may not be an optimal strategy for the intermittent S-start swimmer at a specific undulating period T_s. According

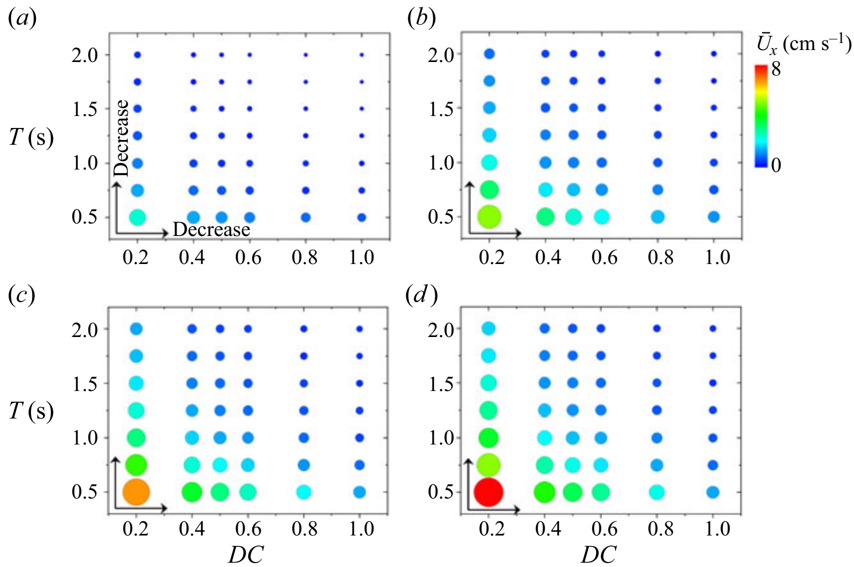

Figure 4. Influence of DC and T on $\bar{U}_x$ with (*a*) $A = 0.05L$, (*b*) $A = 0.10L$, (*c*) $A = 0.15L$, and (*d*) $A = 0.20L$.

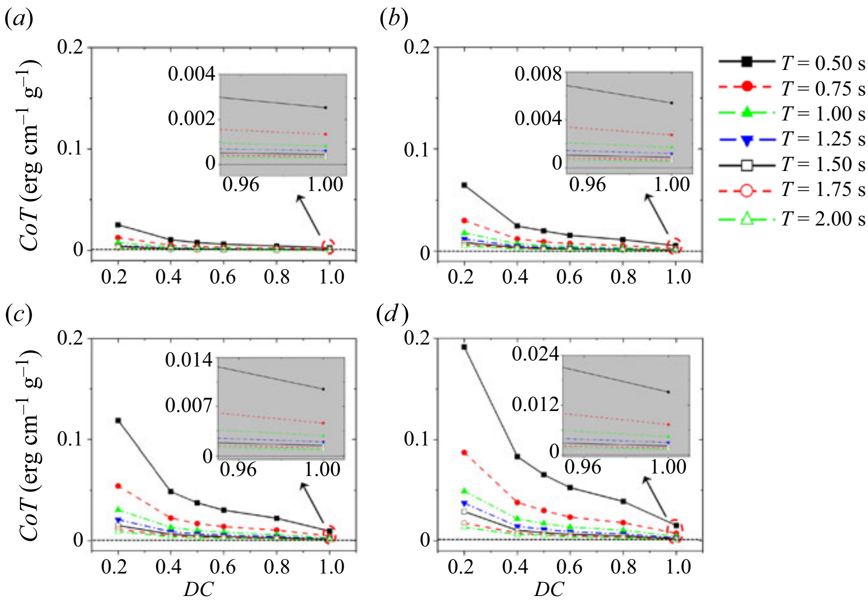

Figure 5. Influence of DC and T on CoT at (*a*) $A = 0.05L$, (*b*) $A = 0.10L$, (*c*) $A = 0.15L$, and (*d*) $A = 0.20L$.

to figure 4, a larger A corresponds to higher swimming speeds, which concurs with previous studies on oscillating, undulating and self-propelling foils (e.g. Floryan, Van Buren & Smits 2019). Overall, $\bar{U}_x$ correlates strongly with A but inversely with DC and T.

The effects of DC, T and A on CoT are shown in figure 5, where CoT decreases with increasing DC and/or T, but it increases with increasing A. As discussed in Chao, Alam & Cheng (2022), an increase in tailbeat amplitude A requires more input power. A larger

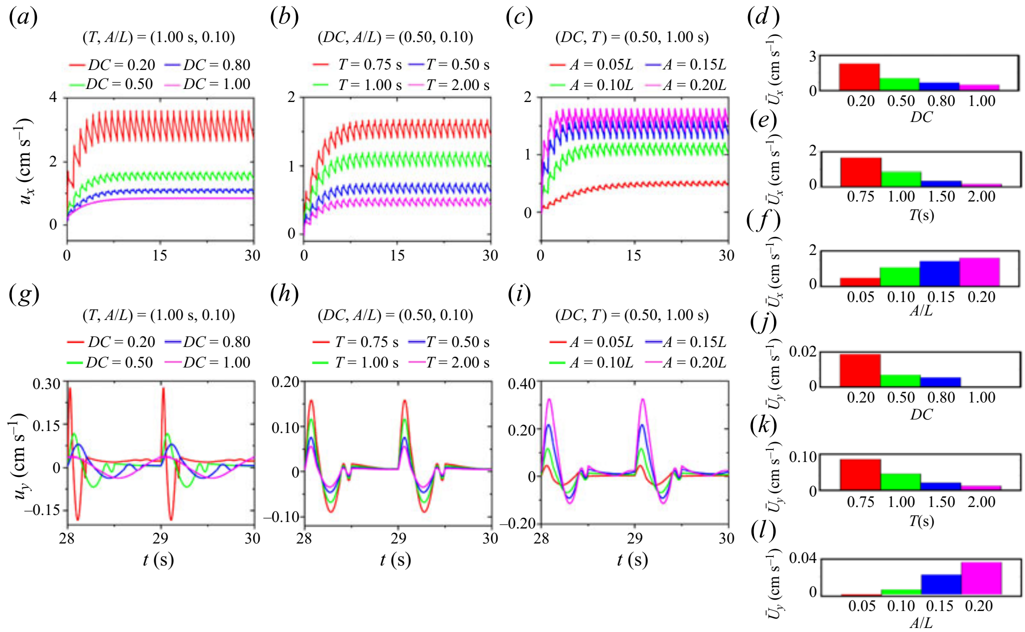

Figure 6. The effect of (*a*) DC, (*b*) T, and (*c*) A on u_x, and (*d–f*) the corresponding steady-state swimming velocities $\bar{U}_x$. The effect of (*g*) DC, (*h*) T, and (*i*) A on u_y, and (*j–l*) the corresponding steady-state lateral velocities $\bar{U}_y$.

value of A also hinders the flow passing around the foil. As a result, increasing A leads to inefficient swimming, i.e. higher CoT. An inverse relationship forms between CoT and DC at specific T and A. This is because a higher undulating frequency (smaller DC) requires more input power. Given a set of (DC, A), the decline of CoT slows down with increasing T. It is desirable to have a lower CoT because it indicates lower energy consumption, thus greater mechanical efficiency. According to figure 5, intermittent S-start swimming results in inefficient propulsion. Floryan *et al.* (2019) found that at a given Strouhal number, the foil efficiency can be increased by increasing the trailing edge amplitude. However, this is not the case for the present self-propelling foil, where CoT increases with an increase in A.

Figure 6 illustrates how examined parameters DC, T and A affect the instantaneous swimming speed in horizontal and vertical directions. As expected, a smaller DC causes significant fluctuations in u_x and u_y at given (T, A) (figures 6*a*,*g*). A continuous swimming mode generates steady forward motion with fewer fluctuations, whereas an intermittent S-start gait leads to higher swimming speeds with larger fluctuations around the mean velocity. In a similar way, a smaller T and a larger A lead to more fluctuating u_x and u_y velocities (figures 6*b*,*c*,*h*,*i*). Interestingly, the u_x curve is stabilized easily with a higher A, whereas $A = 0.05L$ leads to a negative $\bar{U}_y$ (figure 6*l*). This result suggests that an S-start swimmer may adopt smaller DC and T, but a larger A to achieve higher instantaneous and time-averaged speeds (figures 6*a–f*). However, it has been observed from biological experiments that the fish does not tend to produce large amplitudes when adopting an S-start motion. A plausible explanation is that larger tailbeat amplitudes produce high-speed flows (that could reveal the fish's whereabouts) and are costlier energetically. The decision-making behaviour behind this observation deserves further exploration.

3.2. *Scaling laws applicable to intermittent S-start, B-and-C and continuous swimming*

To better understand the effects of swimming parameters DC, T and A on $\bar{U}_x$ and CoT (figures 4 and 5), scaling laws for swimming speed and efficiency are derived. In the previous subsection, we considered variations in both S-start and B-and-C swimming kinematics because T_s and T were varied independently. In terms of scaling laws, we do not distinguish explicitly between the two gaits, and refer to them collectively as S-start or intermittent motions. The scaling laws for hydrodynamic performance metrics are derived by balancing the work done by thrust and drag forces. We note that our starting point for deriving the scaling laws differs from previous studies on continuous swimming that consider force balance instead of energy balance. Due to the differences in duration and intensity of thrust and drag forces between S-start and glide phases of intermittent swimming, a force balance approach is not appropriate. Using the principle of energy balance, we can account explicitly for S-start and glide periods (T_s and T_g, respectively) in scaling laws. According to this, during steady swimming, the energy spent/work done by the thrust force during the S-start phase is used in overcoming the hydrodynamic drag throughout the swimming period. In steady state and over the course of a swimming cycle, the swimmer's kinetic energy remains the same. This is because kinetic energy gained through thrust forces is lost through drag forces. At the end of the cycle, the swimmer achieves the same swimming velocity as when it started (see figure 6). As a result, the kinetic energy term does not appear in the energy balance statement that follows next. We note that the scaling laws that we derive have an input versus output relationship. Inputs to the laws are the foil kinematic parameters, which are known beforehand and do not require computational fluid dynamics simulation. This is different from the velocity scale given in Akoz & Moored (2018) (for an intermittent swimmer), which has a mixed form – that is, it contains both input (foil kinematic parameters) and output (thrust force) quantities, depends on drag and thrust decomposition of the hydrodynamic force, and relies on potential flow theory.

3.2.1. *Scaling laws based on overcoming the viscous drag*

An intermittent swimmer undulates its body at an effective angular frequency $\omega^{eff} = \omega/DC = 2\pi/(DC \times T) = 2\pi/T_s$, with $DC < 1$. Here, $\omega = 2\pi/T$ denotes the angular frequency, T is the total swimming period, and T_s is the flapping time period. During steady swimming in a low to moderate Reynolds number flow regime, the thrust energy is expended overcoming viscous drag, i.e.

$$E_T \sim E_D. \tag{3.1}$$

Here, E_T (henceforth called thrust energy) represents the energy used or work done by thrust forces during the flapping period T_s, and E_D (henceforth called viscous drag energy) represents the energy spent during the entire swimming period, $T = T_s + T_g$, in overcoming viscous drag (figure 1*b*).

The thrust energy can be estimated through thrust force $F_T \sim \rho\, U_{lateral}^2 A_p$ as $E_T \sim F_T \bar{U}_x T_s$. Here, $U_{lateral} = A\omega/DC$ is the deformation velocity in the lateral direction, A is the tailbeat amplitude, and A_p is the projected area of the swimmer into the plane of the paper. Thus, $A_p \sim L \times W$, in which L is the length of the swimmer, and W is the width of the swimmer (into the plane of the paper). Gazzola *et al.* (2014) provide a geometric argument for the thrust force scale for undulatory swimmers. This scale has also been used in prior studies of aquatic locomotion (Bale *et al.* 2014; Floryan, Van Buren & Smits 2018; Floryan *et al.* 2019). The viscous drag energy can be estimated from the viscous drag force F_D as $E_D \sim F_D \bar{U}_x T$. The viscous drag force can be estimated from the Blasius solution $F_D \sim \mu(\bar{U}_x/\delta)A_p$. Here, $\bar{U}_x$ is the steady time-averaged swimming speed, and $\delta \sim L/\sqrt{Re}$ is the boundary layer thickness, with $Re = \bar{U}_x L/\nu$ the Reynolds number. By equating thrust to viscous drag work, we obtain

$$\left.\begin{aligned} E_T &\sim E_D, \\ \rho(A\omega/DC)^2 A_p \bar{U}_x T_s &\sim \frac{\mu \bar{U}_x A_p}{L}\left(\frac{\bar{U}_x L}{\nu}\right)^{1/2} \bar{U}_x (T_s + T_g) \\ \hookrightarrow \bar{U}_x &\sim (A\omega)^{4/3}(DC)^{-2/3} L^{1/3} \nu^{-1/3}, \end{aligned}\right\} \tag{3.2}$$

in which we used the definition $DC = T_s/(T_s + T_g)$. Equation (3.2) can be non-dimensionalized and rewritten succinctly as

$$Re \sim Sw^{4/3}/DC^{2/3}. \tag{3.3}$$

The scaling law for the cost of transport CoT can be derived using its definition and velocity scale (3.2) as

$$\left.\begin{aligned} CoT &= \frac{E_L}{\bar{U}_x T} \\ &\sim \frac{\rho(A\omega/DC)^3 A_p T_s}{(A\omega)^{4/3}(DC)^{-2/3} L^{1/3} \nu^{-1/3} T} \\ \hookrightarrow CoT &\sim \rho \nu^2 (W/L)(Sw)^{5/3}(DC)^{-4/3}, \end{aligned}\right\} \tag{3.4}$$

The numerator of the cost of transport E_L in (3.4) represents the energy spent or work done by the swimmer deforming its body in the lateral direction. Following Bale *et al.* (2014), the lateral power scales as $P_L \sim \rho\, U_{lateral}^3 A_p$. (According to Bale *et al.* (2014), most of the muscle work is done in producing lateral deformations. Consequently, $P_{muscle} \approx P_L$.) Consequently, work done in generating body deformations during the swimming period is $E_L = P_L T_s$. The denominator $\bar{U}_x T$ represents the distance travelled by the swimmer during the swimming period. Equation (3.4) can be non-dimensionalized and rewritten succinctly as

$$C_E = \frac{CoT}{\rho \nu^2}\left(\frac{L}{W}\right) \sim Sw^{5/3}/DC^{4/3}. \tag{3.5}$$

For a two-dimensional swimmer, a unit width is taken into the plane of the swimmer, i.e. $W = 1$.

Equations (3.3) and (3.5) provide a relationship between (non-dimensional) swimming speed Re and energy consumption C_E of the foil as a function of its key kinematic parameters Sw and DC. To see how well the above scaling laws fit the simulated data of the previous section, we plot the foil's measured outputs, Re and C_E, against its kinematic inputs, $Sw^{4/3}/DC^{2/3}$ and $Sw^{5/3}/DC^{4/3}$ in figures 7(*a*,*b*), respectively. It can be observed that the output data for different values of DC collapse well onto a single straight line, suggesting that (3.3) and (3.5) can be used as scaling laws to estimate the hydrodynamic performance of an intermittent S-start swimmer. Furthermore, these two scaling laws also explain the results of the previous section very well. For example, considering a swimmer of fixed length L and time period T, (3.3) suggests that a larger A (thus Sw) leads to a higher $\bar{U}_x$ (figures 6*c*,*f*). Similarly, a smaller DC generates a higher (time-averaged)

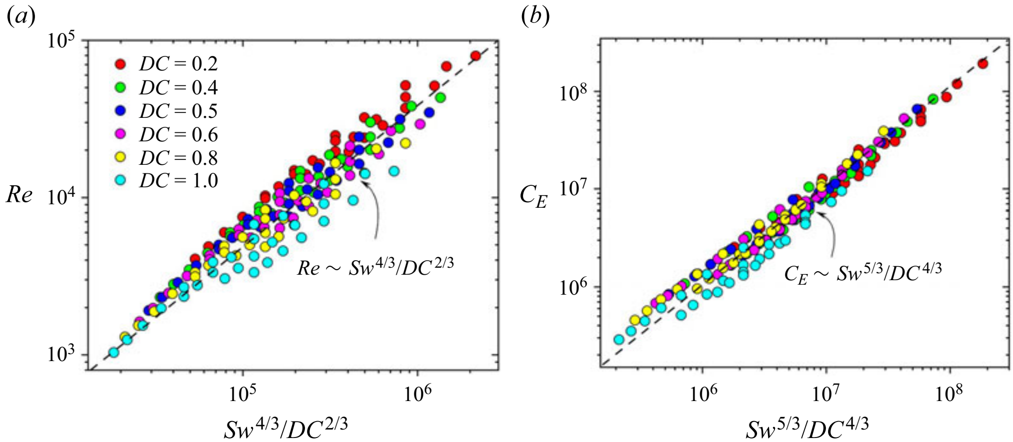

Figure 7. Scaling laws for (*a*) swimming speed *Re*, and (*b*) efficiency C_E, based on overcoming the viscous drag. The fitted dashed lines are $Re = 0.037\, Sw^{4/3}/DC^{2/3}$ and $C_E = 1.032\, Sw^{5/3}/DC^{4/3}$, and the coefficients of determination are $R^2 = 0.889$ and 0.987 for (*a*,*b*), respectively.

swimming speed $\bar{U}_x$ (figures 6*a*,*d*). Equation (3.5) also shows that C_E is inversely related to *DC*, which confirms the hypothesis that intermittent S-start swimming ($DC < 1.0$) is less efficient than the continuous one ($DC = 1.0$).

3.2.2. *Scaling laws based on overcoming the pressure drag*

For high-speed flows, it can be argued that the thrust energy/work E_T is spent in overcoming the pressure drag F_P instead of the viscous drag F_D. For inviscid fluids, this is indeed the case. The pressure force scales as the square of the body's velocity, i.e. $F_P \sim \rho \bar{U}_x^2 A_p$. For a geometric argument for the F_P scale for undulatory swimmers, see Gazzola *et al.* (2014). Thus, by equating thrust to pressure drag work, we obtain

$$\left.\begin{aligned} E_T &\sim E_P, \\ \rho (A\omega/DC)^2 A_p \bar{U}_x T_s &\sim \rho \bar{U}_x^2 A_p \bar{U}_x (T_s + T_g) \\ \hookrightarrow \bar{U}_x &\sim A\omega/DC^{1/2}. \end{aligned}\right\} \tag{3.6}$$

Through non-dimensionalization, we obtain

$$Re \sim Sw/DC^{1/2}. \tag{3.7}$$

The corresponding *CoT* scale is obtained as

$$\left.\begin{aligned} CoT &= \frac{E_L}{\bar{U}_x T} \\ &\sim \frac{\rho (A\omega/DC)^3 A_p T_s}{A\omega (DC)^{-1/2} T} \\ \hookrightarrow CoT &\sim \rho \nu^2 (W/L) Sw^2/DC^{3/2}. \end{aligned}\right\} \tag{3.8}$$

Equation (3.8) can be non-dimensionalized and rewritten as

$$C_E = \frac{CoT}{\rho \nu^2}\left(\frac{L}{W}\right) \sim Sw^2/DC^{3/2}. \tag{3.9}$$

https://doi.org/10.1017/jfm.2024.103 Published online by Cambridge University Press

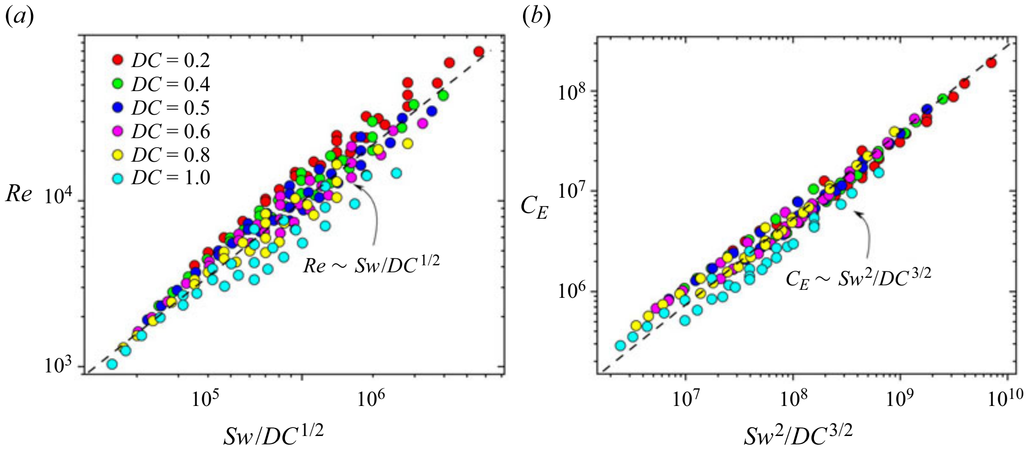

Figure 8. Scaling laws for (*a*) swimming speed *Re*, and (*b*) efficiency C_E, based on overcoming the pressure drag. The fitted dashed lines are $Re = 1.279Sw/DC^{1/2}$ and $C_E = 0.029Sw^2/DC^{3/2}$, and the coefficients of determination are $R^2 = 0.883$ and $R^2 = 0.980$ for (*a*,*b*), respectively.

Equations (3.7) and (3.9) are compatible with inviscid flows as the effect of $\nu \to 0$ is eliminated. According to figure 8, scaling laws based on overcoming the pressure drag are also able to fit the data reasonably well. We attribute this match to the moderate flow regime ($10^3 < Re < 10^5$) considered in this study. At very-low-speed ($Re \sim 1$) and very-high-speed ($Re > 10^6$) flows, we expect to see a more distinct trend between viscous-based and pressure-based scaling laws. At low *Re*, the fluid–structure interaction (FSI) equations are coupled strongly, while at high *Re*, explicit turbulence models are required to resolve the turbulent flow features. In our flow solver, we solve the FSI equations in a split manner without explicit turbulence models, which is suitable for simulating moderate-*Re* FSI cases. The two scaling laws will be tested in low- and high-speed flow regimes in a future study. Because we are considering moderate *Re* flows in this study, we prefer viscous scaling laws over pressure-based ones to describe the hydrodynamic performance of intermittent S-start swimmers (speed and efficiency). To validate whether the data statistically support the different scaling laws that have been presented, we have conducted t-tests on the scaling laws.

In order to check whether the data support the different scaling laws presented in this section, we performed t-tests on the data. We assume that the data fit power laws of the form $Re = c_1 Sw^{\alpha_1} DC^{\alpha_2}$ and $C_E = c_2 Sw^{\alpha_3} DC^{\alpha_4}$. Using ordinary least squares regression on the data, the coefficients obtained were $\alpha_1 = 0.9829$, $\alpha_2 = -0.8928$, $\alpha_3 = 1.7833$ and $\alpha_4 = -1.2453$. After that, two-sample t-tests were performed on the statistical values of *Re* and C_E, as well as their simulation values, at a significance level of 0.05. As expected, the means of the data sets were equal and the statistics converged to the simulation values. We accept the null hypothesis at significance level 0.05. Table 4 and table 5 present the least squares regression fit and two-sample t-test results, respectively.

3.2.3. *Special cases of $DC \to 0$ and $DC \to 1$*

The two cases $DC \to 0$ and $DC \to 1$ warrant separate discussion. The swimmer reaches $DC \to 0$ if: (i) it does not flap its body at all; (ii) its gliding period is much longer than its flapping period, i.e. $T_g \gg T_s$; or (iii) it flaps infinitely fast in an infinitely short period of time. The first two scenarios imply that $Sw \to 0$. It follows that the body's steady

	α_1	α_2	α_3	α_4
Value	0.9829	−0.8928	1.7833	−1.2453
Standard error	0.0173	0.0192	0.0159	0.0147

Table 4. Values and standard errors in $\{\alpha_i\}$ obtained using the ordinary least squares regression.

	t-statistic	Degrees of freedom	Standard error	p-value
Re	0.025673	334	0.001405	0.979533
C_E	0.032521	334	0.001779	0.974076

Table 5. Results of t-tests between the simulation and statistical values of Re and C_E.

swimming velocity and energy expenditure should also approach zero when $DC \to 0$. The viscous and pressure scaling laws discussed in §§ 3.2.1 and 3.2.2 lead naturally to this conclusion. These laws are in the form Sw^m/DC^n, with $m > n$ and $m, n \in \mathbb{R}^+$. As $DC^n \to 0$, $Sw^m \to 0$ at a faster rate, which leads to the expected result. The third scenario is unphysical, as there is a practical limitation to how rapidly a body can flap. For example, Sanchez-Rodriguez, Raufaste & Argentina (2023) mentioned that an undulatory swimmer's tailbeat frequency is generally less than 20 Hz. Also, a very fast oscillation in a very short amount of time breaks the local thermodynamic equilibrium assumption of fluid mechanics, which requires that flow quantities (velocity, pressure) change at a reasonable rate (Jakobsen 2008). Thus scenario (iii) is not considered in the scaling laws derived in this work. (Moreover, it seems impossible to obtain experimental or simulation data to validate some candidate scaling law in this situation.)

The other end of the DC range, $DC \to 1$, implies continuous swimming. It can be observed that as $DC \to 1$, the scaling laws derived for the inertial flow regime reduce to $Re \sim Sw$ and $C_E \sim Sw^2$, whereas those obtained for the viscous flow regime reduce to $Re \sim Sw^{4/3}$ and $C_E \sim Sw^{5/3}$. For both flow regimes, our results are consistent with the scaling laws for steady, continuous swimming velocity derived in Gazzola *et al.* (2014).

3.3. *Wake structures*

In figure 9(*a*), six different flow patterns are illustrated, including 2P (◇), 2P+S (□), 2S (■), Mode I (○), Mode II (△) and Mode III wake (▽). At smaller DC and Sw, i.e. the bottom left corner in the DC–Sw plane, two vortex pairs (2P) are generated by the S-start phase, and a single vortex (S) is generated by the boundary layer separation in the gliding phase (figure 9*b*). Increasing DC decreases the time lag between adjacent S-start phases, thereby suppressing boundary layer separation. Consequently, only two vortex pairs are observed as 2P wakes (figure 9*c*) when $Sw \leq 3000$ and $0.5 \leq DC < 1.0$. Further, for the 2P+S wake, the single vortex located in the middle of two vortex pairs gradually approaches and merges with the upper vortex pair (figure 9*b*). In the far field, therefore, the 2P+S wake would eventually become a 2P wake. Figure 9(*a*) illustrates a bifurcation caused by the 2P+S and 2P wake behind the foil at smaller Sw. A typical 2S reverse Kármán vortex street appears at $DC = 1.0$ (figure 9*d*).

By increasing Sw (by increasing either A or T), a blurry flow pattern, i.e. Mode I and Mode II wakes, appears gradually at $DC \leq 0.5$. There are four types of vortex structures

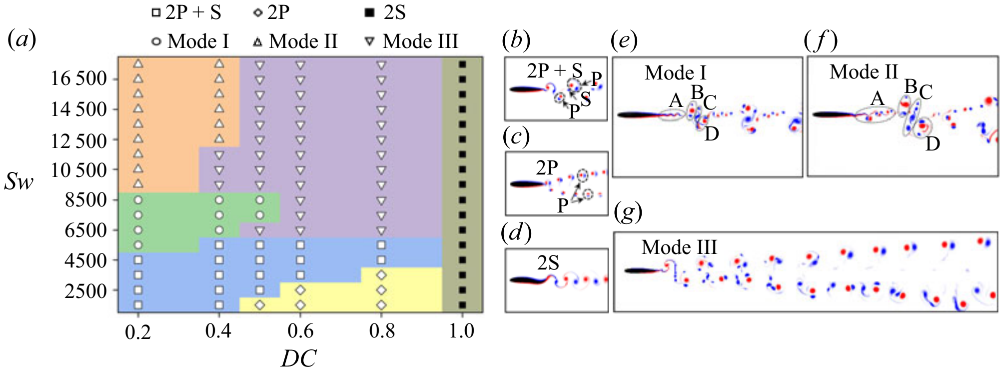

Figure 9. (*a*) Flow patterns in the *DC*–*Sw* plane. (*b*–*g*) Typical wake structures. Red and blue denote positive and negative vorticity, respectively.

in the Mode I and Mode II wakes: A, B, C and D (figures 9*e*,*f*). The vortex structure A corresponds to the boundary layer separation in the gliding phase, forming nS and mP+nS structures in the Mode I and Mode II wakes, respectively (Williamson & Roshko 1988). The vortex structures B, C and D are generated during the S-start phase. The vortex structure B in the Mode I and Mode II wakes is similar, where a strong positive vortex is surrounded by two weak negative vortices. The vortex structure C contains several negative vortices, with the Mode II wake providing more single vortex structures compared to the Mode I wake; see figure 9(*f*). The blurry vortex structure D describes the interaction between vorticity produced by the S-start phase and the one produced by the gliding phase. The evolution of Mode I and Mode II wakes due to the intermittent motion of a pitching foil has also been reported in Akoz *et al.* (2019), where it is mentioned that vortex structures B and D increase the swimming velocity, whereas structure C causes a deceleration. The Mode III wake occupies a large portion of the *DC*–*Sw* plane. After a series of vortex mergers, the Mode III wake eventually becomes a 2P wake, as shown in figure 9(*g*).

4. Conclusions

In this work, intermittent S-start swimming is studied in a systematic manner. The numerical study reveals that the time-averaged swimming velocity $\bar{U}_x$ and the cost of transport *CoT* increase with decreasing duty cycle *DC*. This suggests that although intermittent S-start swimming leads to higher swimming speeds (which is good for both escaping predators and striking prey), it is an inefficient swimming gait compared to continuous cruising. We also presented two scaling laws to characterize the hydrodynamic performance of S-start swimmers, $Re \sim Sw^{4/3}/DC^{2/3}$ and $C_E \sim Sw^{5/3}/DC^{4/3}$, which are suitable for moderate speed flows ($10^3 < Re < 10^5$) considered in this work. During swimming, hydrodynamic performance can be measured by *Re* and C_E, which represent swimming speed and energy consumption. We can use *Sw* and *DC* to measure kinematic inputs for the swimmer. At high $Re > 10^6$, we expect the hydrodynamic performance metrics to scale as $Re \sim Sw/DC^{1/2}$ and $C_E \sim Sw^2/DC^{3/2}$, although this needs to be verified. Additionally, we also classified the wake structures of self-propelling intermittent S-start swimmers in this work. Finally, we note that the plots relating to scaling results appear to be stratified according to *DC*: points with higher *DC* values lie beneath points with lower *DC* values. A similar stratification is also found in the work of Akoz & Moored

(2018) (see their figure 10). Perhaps the scaling relations do not quite capture *DC* effects, and this motivates further investigation.

Supplementary movie. A supplementary movie is available at https://doi.org/10.1017/jfm.2024.103.

Acknowledgements. The authors thank the anonymous reviewers for their insightful comments and careful analysis of the scaling laws, which improved this work.

Funding. J.W. acknowledges the support of the National Natural Science Foundation of China (grant no. 12072158) and the Natural Science Foundation of Jiangsu Province (grant no. BK20231437). This work is also supported by the Priority Academic Program Development of Jiangsu Higher Education Institutions (PAPD). K.K. and A.P.S.B. acknowledge the support of United States National Science Foundation Award OAC 1931368.

Declaration of interests. The authors report no conflict of interest.

Author ORCIDs.
- Dewu Yang https://orcid.org/0000-0002-5809-2361;
- Jie Wu https://orcid.org/0000-0001-6963-0244;
- Kaustubh Khedkar https://orcid.org/0000-0002-9773-5577;
- Li-Ming Chao https://orcid.org/0000-0002-8800-6065;
- Amneet Pal Singh Bhalla https://orcid.org/0000-0002-0173-9881.

REFERENCES

AKOZ, E., HAN, P., LIU, G., DONG, H. & MOORED, K.W. 2019 Large-amplitude intermittent swimming in viscous and inviscid flows. *AIAA J.* **57**, 3678–3685.

AKOZ, E. & MOORED, K.W. 2018 Unsteady propulsion by an intermittent swimming gait. *J. Fluid Mech.* **834**, 149–172.

ASHRAF, I., WASSENBERGH, S.V. & VERMA, S. 2021 Burst-and-coast swimming is not always energetically beneficial in fish (*Hemigrammus bleheri*). *Bioinspir. Biomim.* **16**, 016002.

BALE, R., HAO, M., BHALLA, A.P.S. & PATANKAR, N.A. 2014 Energy efficiency and allometry of movement of swimming and flying animals. *Proc. Natl Acad. Sci. USA* **111**, 7517–7521.

BHALLA, A.P.S., BALE, R., GRIFFITH, B.E. & PATANKAR, N.A. 2013*a* A unified mathematical framework and an adaptive numerical method for fluid–structure interaction with rigid, deforming, and elastic bodies. *J. Comput. Phys.* **250**, 446–476.

BHALLA, A.P.S., GRIFFITH, B.E. & PATANKAR, N.A. 2013*b* A forced damped oscillation framework for undulatory swimming provides new insights into how propulsion arises in active and passive swimming. *PLoS Comput. Biol.* **9** (6), e1003097.

BORAZJANI, I., SOTIROPOULOS, F., TYTELL, E.D. & LAUDER, G.V. 2012 Hydrodynamics of the bluegill sunfish C-start escape response: three-dimensional simulations and comparison with experimental data. *J. Expl Biol.* **215**, 671–684.

BRETT, J.R. & SUTHERLAND, D.B. 1965 Respiratory metabolism of pumpkinseed (*Lepomis gibbosus*) in relation to swimming speed. *J. Fish. Board Canada* **22** (2), 405–409.

CHAO, L.-M., ALAM, M.M. & CHENG, L. 2022 Hydrodynamic performance of slender swimmer: effect of traveling wavelength. *J. Fluid Mech.* **947**, A8.

CHUANG, M.-H. 2009 On burst-and-coast swimming performance in fish-like locomotion. *Bioinspir. Biomim.* **4**, 036001.

DAI, L., HE, G., ZHANG, X. & ZHANG, X. 2018 Intermittent locomotion of a fish-like swimmer driven by passive elastic mechanism. *Bioinspir. Biomim.* **13**, 056011.

DOMENICI, P. & BLAKE, R.W. 1997 The kinematics and performance of fish fast-start swimming. *J. Expl Biol.* **200**, 1165–1178.

FLORYAN, D., VAN BUREN, T. & SMITS, A.J. 2017 Forces and energetics of intermittent swimming. *Acta Mechanica Sin.* **33**, 725–732.

FLORYAN, D., VAN BUREN, T. & SMITS, A.J. 2018 Efficient cruising for swimming and flying animals is dictated by fluid drag. *Proc. Natl Acad. Sci. USA* **115**, 8116–8118.

FLORYAN, D., VAN BUREN, T. & SMITS, A.J. 2019 Large-amplitude oscillations of foils for efficient propulsion. *Phys. Rev. Fluids* **4**, 093102.

Gazzola, M., Argentina, M. & Mahadevan, L. 2014 Scaling macroscopic aquatic locomotion. *Nat. Phys.* **10**, 758–761.

Gazzola, M., Rees, W.M.V. & Koumoutsakos, P. 2012 C-start: optimal start of larval fish. *J. Fluid Mech.* **698**, 5–18.

Gleiss, A.C., *et al.* 2011 Convergent evolution in locomotory patterns of flying and swimming animals. *Nat. Commun.* **2**, 352.

Griffith, B.E. 2009 An accurate and efficient method for the incompressible Navier–Stokes equations using the projection method as a preconditioner. *J. Comput. Phys.* **228**, 7565–7595.

Griffith, B.E. & Patankar, N.A. 2020 Immersed methods for fluid–structure interaction. *Annu. Rev. Fluid Mech.* **52**, 421–448.

Gupta, S., Thekkethil, N., Agrawal, A., Hourigan, K., Thompson, M.C. & Sharma, A. 2021 Body-caudal fin fish-inspired self-propulsion study on burst-and-coast and continuous swimming of a hydrofoil model. *Phys. Fluids* **33**, 091905.

Hoover, A.P., Cortez, R., Tytell, E.D. & Fauci, L.J. 2018 Swimming performance, resonance and shape evolution in heaving flexible panels. *J. Fluid Mech.* **847**, 386–416.

Jakobsen, H.A. 2008 *Chemical Reactor Modeling. Multiphase Reactive Flows*. Springer.

Li, G., Ashraf, I., Francois, B., Kolomenskiy, D., Lechenault, F., Godoy-Diana, R. & Thiria, B. 2021 Burst-and-coast swimmers optimize gait by adapting unique intrinsic cycle. *Commun. Biol.* **4**, 40.

Li, G., Muller, U.K., van Leeuwen, J.L. & Liu, H. 2014 Escape trajectories are deflected when fish larvae intercept their own C-start wake. *J. R. Soc. Interface* **11**, 20140848.

Liu, K., Huang, H. & Lu, X.-Y. 2020 Hydrodynamic benefits of intermittent locomotion of a self-propelled flapping plate. *Phys. Rev.* E **102**, 053106.

Patel, N.K., Bhalla, A.P.S. & Patankar, N.A. 2018 A new constraint-based formulation for hydrodynamically resolved computational neuromechanics of swimming animals. *J. Comput. Phys.* **375**, 684–716.

Sanchez-Rodriguez, J., Raufaste, C. & Argentina, M. 2023 Scaling the tail beat frequency and swimming speed in underwater undulatory swimming. *Nat. Commun.* **14** (1), 5569.

Triantafyllou, M.S. 2012 Survival hydrodynamics. *J. Fluid Mech.* **598**, 1–4.

Triantafyllou, M.S., Weymouth, G.D. & Miao, J. 2016 Biomimetic survival hydrodynamics and flow sensing. *Annu. Rev. Fluid Mech.* **48**, 1–24.

Tytell, E.D., Leftwich, M.C., Hsu, C.-Y., Griffith, B.E., Cohen, A.H., Smits, A.J., Hamlet, C. & Fauci, L.J. 2016 Role of body stiffness in undulatory swimming: insights from robotic and computational models. *Phys. Rev. Fluids* **1**, 073202.

Videler, J.J. & Hess, F. 1984 Fast continuous swimming of two pelagic predators, saithe (*Pollachius virens*) and mackerel (*Scomber scombrus*): a kinematic analysis. *J. Expl Biol.* **109**, 209–228.

Weihs, D. 1973 The mechanism of rapid starting of slender fish. *Biorheology* **10**, 343–350.

Williamson, C.H.K. & Roshko, A. 1988 Vortex formation in the wake of an oscillating cylinder. *J. Fluid Struct.* **2**, 355–381.